Rare Metal Materials and Engineering
Volume.50, Issue.4, April 2021
Available online at **www.rmme.ac.cn**

Science Press

Cite this article as: Zhou Xuan,Wang Kelu,Lu Shiqiang,et al.Hot Deformation Behavior of Ti2041 Alloy Based on BP Neural Network and 3D Processing Map[J].Rare Metal Materials and Engineering,2021,50(04):1233-1240.

Hot Deformation Behavior of Ti2041 Alloy Based on BP Neural Network and 3D Processing Map

Zhou Xuan[1], Wang Kelu[1], Lu Shiqiang[1], Li Xin[1], Ouyang Delai[2]

[1] School of Aeronautical Manufacturing Engineering, Nanchang Hangkong University, Nanchang 330063, China; [2] School of Materials Science and Engineering, Nanchang Hangkong University, Nanchang 330063, China

Abstract: The flow behavior of Ti2041 alloy was studied through hot compressive experiments. The constitutive model of alloy was established by back propagation (BP) neural network. Results show that the constitutive model has high accuracy, with correlation coefficient of 0.996 13 and average relative error of 4.498%, and the data points whose predictive deviation is within 10% are 92.98%. Based on the experimental data, the strain rate sensitivity, the power dissipation and the instability parameter were investigated. Processing maps were established. Through processing map prediction and microstructure observation, the instability zones are mainly flow localization (650~775 ℃/0.056~1 s^{-1}) and mechanical instability (825~900 ℃/0.056~1 s^{-1}), and the deformation mechanism of the stability zone is mainly dynamic recrystallization. It is found that the optimal deformation parameters are: deformation temperature of 760~825 ℃/825~900 ℃ and strain rate of 0.001~0.01 s^{-1}/0.0032~ 0.056 s^{-1}.

Key words: Ti2041 alloy; flow stress; constitutive model; processing maps; optimal processing parameters

β titanium alloy has excellent properties such as low density, biocompatibility, corrosion resistance and high specific strength, which is widely used in aerospace, automobile, medical equipment and other fields[1-3]. Ti2041 alloy belongs to a new type β titanium alloy, which is developed by Sumitomo Metal Industries of Japan. The alloy has excellent cold working properties and can obtain high strength and high toughness after proper aging treatment. At the same time, it can also control the strength-plasticity matching of the alloy by proper hot working, and has become a high strength titanium alloy with great development potential. That is to say, reasonable selection of deformation process parameters can improve the processing performance of materials, control the microstructure of materials, and effectively avoid hot working defects [4].

In recent years, some constitutive relationships, such as phenomenological, physical-based and artificial neural network (ANN) models [5], have been widely used. Among these constitutive models, phenomenological constitutive equations and ANN model are widely used in the calculation of flow stress of alloy at high temperatures, because the complex physical metallurgy mechanisms cannot be considered. Ma et al[6]established the constitutive relationship of BT25 titanium alloy based on regression and ANN methods. The results show that the prediction results of ANN model are in good agreement with the experimental data. Li et al[7]established the constitutive relationship of 28CrMnMoV steel based on constitutive equation and ANN model. The results show that the prediction results of ANN model are more efficient and accurate in predicting the flow behavior of 28CrMnMoV steel than the constitutive equations. Huang et al [8]established the strain-compensation Arrhenius, back propagation ANN and optimized back propagation (BP) neural network models based on genetic algorithm (GA). The results show that the optimized BP-ANN model can accurately and reliably predict the flow behavior of 5754 aluminum alloy. Lin et al [9] proposed the strain-compensated Arrhenius, Hensel-Spittel and artificial neural network models to accurately predict the flow behavior of TC18. The results show that the prediction accuracy of artificial neural network model is the best among three constitutive models.

Received date: April 09, 2020
Foundation item: National Natural Science Foundation of China (51761029, 51864035)
Corresponding author: Wang Kelu, Ph. D., Professor, School of Aeronautical Manufacturing Engineering, Nanchang Hangkong University, Nanchang 330063, P. R. China, Tel: 0086-791-83863039, E-mail: wangkelu@126.com

The dynamic material model and its processing map technology have been widely used, and provide an important theoretical basis for a practical application. 3D processing map can directly reflect the change rule of each parameter, and it is also gradually used in the research of hot deformation behavior of metal materials, such as magnesium alloy [10], aluminum alloy [11], titanium alloy [12].

At present, the research on constitutive relation and processing map of Ti2041 alloy is still very limited. In this study, the hot deformation behavior of Ti2041 alloy was studied by hot compression experiments. Based on the measured flow stress curves, the BP ANN models are constructed to estimate the flow stresses. The processing map was constructed by the DMM theory, and the microstructure of the processing map was verified by microstructures in order to optimize the hot forming process parameters of the alloy.

1 Experiment

The experimental material was Ti2041 alloy, and its main chemical composition (wt%) was 20V, 4Al, 1Sn, and balance Ti. The original microstructure is shown in Fig. 1a. Fig. 1b is different deformation areas of the compression specimen. The isothermal compression experiment of Ti2041 alloy was conducted on Gleeble-3800 thermomechanical simulator at the temperatures of 650, 700, 750, 800, 850 and 900 ℃ and the strain rates of 0.001, 0.01, 0.1 and 1 s^{-1}. The specimen size is Φ8 mm×12. All specimens were subjected to 60% height reduction. After hot compression experiments, the deformed specimens were cut along the axial cross-section. The metallographic specimens were ground, polished, dried and then corroded with 10% HF, 30% HNO_3 and 60% H_2O mixture. The microstructures of large deformation areas were characterized by the XJP-6A metallographic microscope.

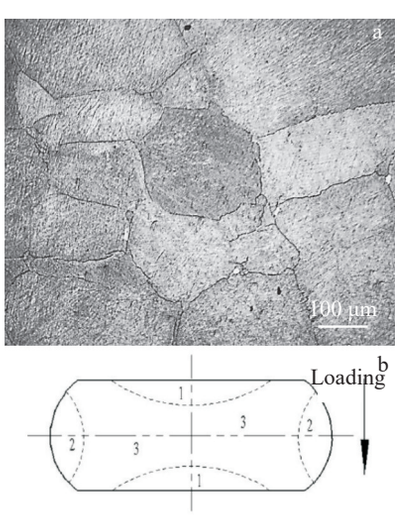

Fig.1 Original microstructure of Ti2041 alloy (a) and deformation areas (1-difficult deformation area; 2-small deformation area; 3-large deformation area) of the compression specimen (b)

2 Flow Behavior of Ti2041 Alloy

Fig. 2 is the flow curve of Ti2041 alloy at deformation temperature of 650~900 ℃ and strain rate of 0.001~1 s^{-1}. In the early stage of deformation, the flow stress increases with the increase of true strain due to dislocation entanglement and pile up caused by work hardening. After that, the flow stress reaches the peak value. Then, the flow stress gradually decreases with the increase of true strain. The reason is that the flow softening rate of DRX and DRV is higher than the work hardening efficiency. Finally, it can be seen that with the increase of deformation temperature and the decrease of strain rate, the flow stress tends to a stable value. The reason is that the work hardening and flow softening reach the dynamic equilibrium and the change of flow stress is not obvious with the increase of true strain under the deformation temperature and strain rate [13,14].

Fig. 3 shows the change rule of peak stress with deformation temperature and strain rate of Ti2041 alloy. The peak stress increases with the decrease of deformation temperature and the increase of strain rate. The reason is that when the deformation temperature is constant, the increase of strain rate will shorten the hot deformation time of the material and make the dynamic recrystallization softening behavior of the alloy inadequate, resulting in the increase of flow stress. When the strain rate is constant, with the increase of deformation temperature, the density of dislocations will decrease due to the increase of atomic motion and dislocation climbing or sliding ability, resulting in the decrease of flow stress.

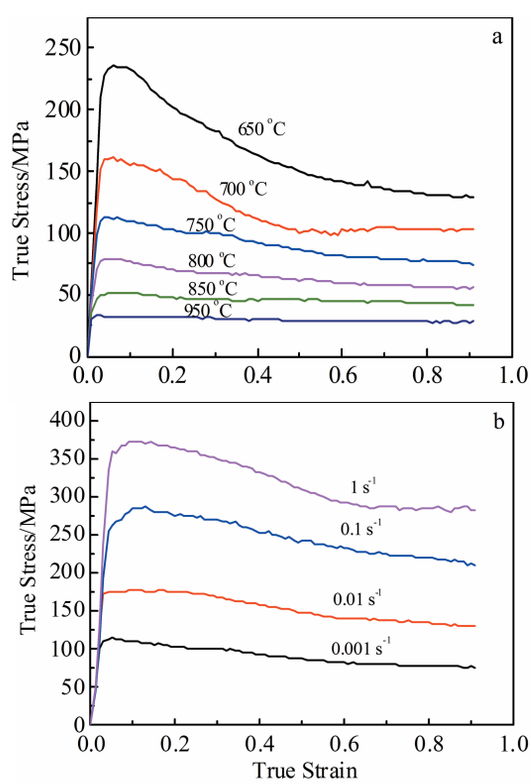

Fig.2 True stress-true strain curves of Ti2041 alloy: (a) $\dot{\varepsilon}$=0.001 s^{-1} and (b) T=750 ℃

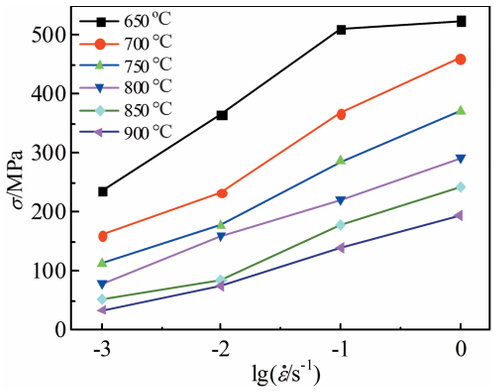

Fig.3 Change of peak stress (σ) with strain rate and deformation temperature of Ti2041 alloy

3 BP ANN Model

ANN is a kind of information processing technology based on human nervous system, and is a successful method to predict non-liner relationships. ANN consists of an input layer, one or more hidden layers and an output layer. The transfer functions are used to connect different layers. At present, there are various ANN models, such as perception model, linear neural network, radial basis function (RBF) network. Among the existing ANN models, BP ANN is an effective method to describe the high temperature deformation behavior.

The sigmoid function described as Eq.(1) is employed as the transfer function in the hidden layer, and the output layer employs the linear function as the transfer function.

$$F(x) = 1/[1 + \exp(-x)] \quad (1)$$

Here, the inputs are temperature, strain and strain rate, the output layer is flow stress. According to the method mentioned in Ref.[15], the trained BP ANN can accurately predict the flow stresses of alloys when the architecture of ANN is 3-5-1, as shown in Fig.4.

In this study, the sample classification of Ti2041 alloy is shown in Table 1. T is the test data and C is the training data. At the beginning of training BP ANN, for improving the accuracy of BP ANN, the input and output parameters for training samples need to be normalized through Eq.(2).

$$N_i = 0.8\left|\frac{N_i' - N_{\min}}{N_{\max} - N_{\min}}\right| + 0.1 \quad (2)$$

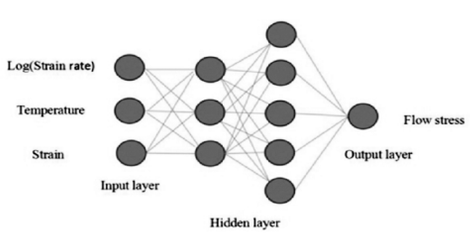

Fig.4 Structure of BP ANN model

Table 1 Sample classification of Ti2041 alloy

$\dot{\varepsilon}$/s^{-1}	Temperature, T/℃					
	650	700	750	800	850	900
0.001	C	T	C	T	C	T
0.01	T	C	T	C	T	C
0.1	C	T	C	T	C	T
1	T	C	T	C	T	C

where N_i' is experimental data; $N_{\min}$ and $N_{\max}$ are the minimum and maximum values of N, respectively. The predicted flow stresses by the BP ANN model accord well with the experimental ones, as shown in Fig.5.

The correlation coefficient (R) and (E) of each model are computed through Eq. (3) and Eq. (4) respectively to further compare the prediction accuracy of the model[16].

$$R = \frac{\sum_{i=1}^{N}(C_i - \bar{C})(T_i - \bar{T})}{\sqrt{\sum_{i=1}^{N}(C_i - \bar{C})^2}\sqrt{\sum_{i=1}^{N}(T_i - \bar{T})^2}} \quad (3)$$

$$E = \frac{\sum_{i=1}^{N}\left|\frac{C_i - T_i}{C_i}\right| \times 100\%}{N} \quad (4)$$

where C_i is the measured stress; T_i is the predicted stress; $\bar{C}$ and $\bar{T}$ are the average values of measured and predicted flow stresses, respectively.

Generally, if R is closer to 1 and the E is smaller, the predicted flow stress will be more accurate [17]. As shown in Fig.6, the R value of BP neural network model is 0.996 13, and the E value is 4.498%. The data points whose predicted value is in the range of 10% reach 92.98%. The BP ANN model has the best prediction accuracy.

4 Establishment of Processing Map

4.1 Principles of processing map

The processing map combines an instability map with a power dissipation efficiency map. Based on the dynamic material model (DMM), the dissipated power (P) containing two sections of integrals can be calculated according to Eq.(5).

$$P = \sigma\dot{\varepsilon} = G + J = \int_0^{\dot{\varepsilon}}\sigma d\dot{\varepsilon} + \int_0^{\sigma}\dot{\varepsilon}d\sigma \quad (5)$$

where the G content refers to the power generated by temperature rise while the J co-content represents the power dissipated by microstructure evolution [18].

Flow stresses can be described as:

$$\sigma = K\dot{\varepsilon}^m \quad (6)$$

where K is constant, m is strain rate sensitivity applied to divide power into G content and J co-content [19, 20]:

$$m = \frac{dJ}{dG} = \frac{\dot{\varepsilon}d\sigma}{\sigma d\dot{\varepsilon}} = \left[\frac{\partial(\ln\sigma)}{\partial(\ln\dot{\varepsilon})}\right]_{T,\varepsilon} = \left[\frac{\partial(\lg\sigma)}{\partial(\lg\dot{\varepsilon})}\right]_{T,\varepsilon} \quad (7)$$

J co-content can be expressed as:

$$J = \int_0^{\sigma}\dot{\varepsilon}d\sigma = \frac{m}{m+1}\sigma\dot{\varepsilon} \quad (8)$$

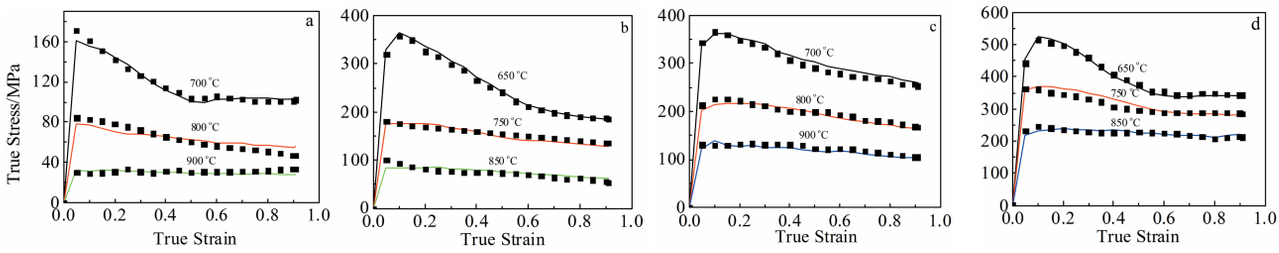

Fig.5 Comparisons between the measured and predicted flow stresses by BP ANN model under different deformation conditions: (a) 0.001 s^{-1}, (b) 0.01 s^{-1}, (c) 0.1 s^{-1} and (d) 1 s^{-1}

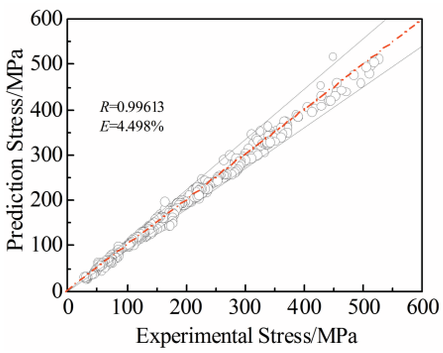

Fig.6 Correlations between the measured and predicted flow stresses by BP ANN model

For an ideal linear dissipation process, m=1 and $J_{max} = \sigma\dot{\varepsilon}/2$.

The power dissipation efficiency η is introduced to evaluate the power-dissipation capacity of the material, represented as [21, 22]:

$$\eta = \frac{J}{J_{max}} = \frac{2m}{m+1} \quad (9)$$

A model considering the appearance of flow instabilities can be expressed according to one dimensionless parameter (ξ) [23, 24]:

$$\xi = \frac{\partial \lg [\, m/(m+1)\,]}{\partial \lg \dot{\varepsilon}} + m<0 \quad (10)$$

The instability map is divided into two parts by ξ, and the processing zone where ξ< 0 is distinguished as instability zone while other part is regarded as safe zone.

The processing map can be obtained by superposing the power dissipation map and the instability map.

4.2 Strain rate sensitivity

For hot processing maps, the efficiency of power dissipation (η) is a function of strain rate sensitivity (m), and instability criterion is also an expression including m simultaneously, suggesting that m is one of the crucial factors. The relationship between strain rate sensitivity and temperature at different strains is constructed, as shown in Fig.7. With the increase of strain, the rules of the m values along with temperature have relatively smaller fluctuations at strain rates of 0.01 and 0.1 s^{-1}. But the change of m values along with temperature have large fluctuations at strain rates of 0.001 and 1 s^{-1}. Moreover, it is also seen that the m values reach the maximum value at the temperature of 800 ℃ and the strain rate of 0.001 s^{-1}. For most metals or alloys, the microstructure such as the grain size, always changes during high temperature deformation, leading to the corresponding change of m values. In general, the grains coarsening and void generation will lead to the decrease of m values, while the grain refinement and the temperature rise caused by deformation heat will lead to the increase of m values [25,26].

4.3 Power dissipation efficiency

The power dissipation efficiency reflects the dynamic change of the structure. The relationship between power dissipation efficiency and temperature at different strains is constructed, as shown in Fig.8. Viewed as a whole, the change of η value is not obviously regular. Some scholars have also reached this conclusion[27,28]. With the increase of strain, the rules of the η value along with temperature have smaller fluctuations at strain rates of 0.01 and 0.1 s^{-1}. But the values of η along with temperature have large fluctuations at strain rates of 0.001 and 1 s^{-1}. However, at the temperature of 800 ℃ and the strain rate of 0.001 s^{-1}, the η values are the highest at different strains, indicating that the hot workability of the material in this zone is better.

Fig.9 displays the three-dimensional distribution diagram of the power dissipation efficiency changing with deformation temperatures, strain rates and strains. At the temperature of 750~825 ℃/850~900 ℃ and the strain rate of 0.001~0.01 s^{-1}/0.001~0.1 s^{-1}, the power dissipation efficiency values are higher. With the increase of strain, the zones with higher power dissipation efficiency values increase. At the temperature of 650~775 ℃ and the strain rate of 0.32~1 s^{-1}, the power dissipation efficiency values are low. With the increase of strain, the zones with low power dissipation efficiency decrease.

4.4 Instability parameter

The instability parameters are the basis for judging the occurrence of structural defects during hot processing (such as wedge cracks, adiabatic shear band, flow localization). As shown in Fig.10, the relationship between instability parameters ξ and temperature at different strains is constructed. Viewed as a whole, with the increase of strain, the rules of the ξ values changing with temperature have smaller undulation at strain rates of 0.001, 0.01 and 0.1s^{-1}. However, the change of ξ values along with temperature has large fluctuations at strain rates of 1 s^{-1}. The ξ values in the group of low

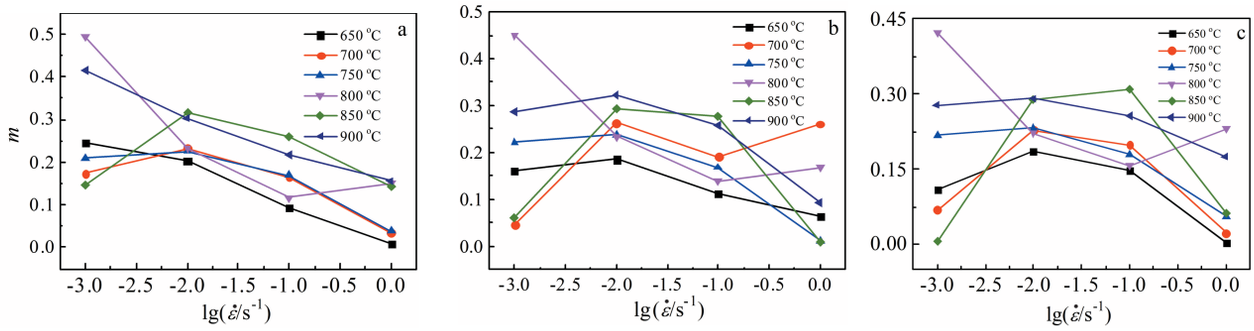

Fig.7 Influence of hot processing parameters on the value of m at different strains: (a) 0.3, (b) 0.6, and (c) 0.9

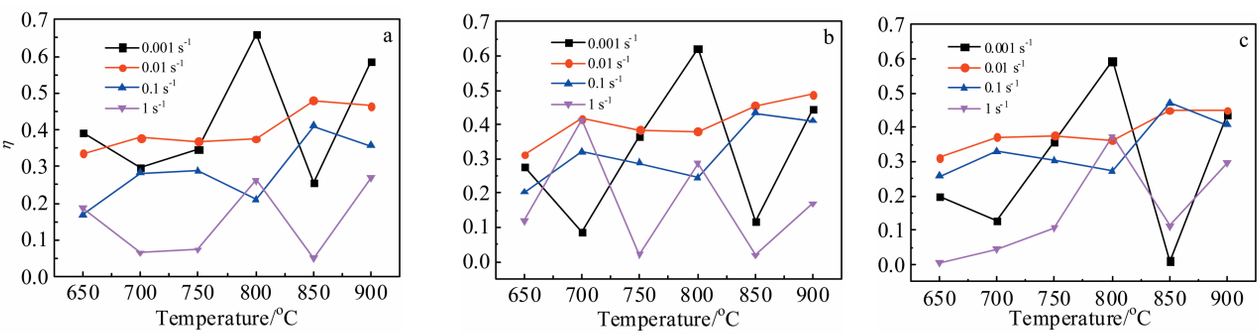

Fig.8 Influence of hot processing parameters on the value of η at different strains: (a) 0.3, (b) 0.6, and (c) 0.9

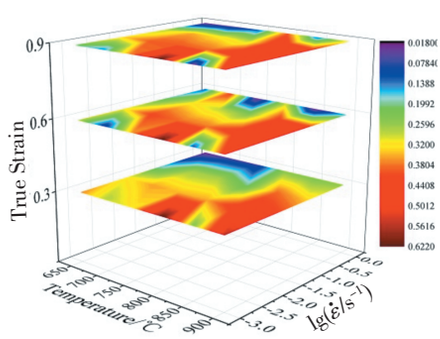

Fig.9 3D power dissipation efficiency diagram of Ti2041 alloy

strain rates (0.001 and 0.01 s^{-1}) are higher than that at high strain rates (1 and 0.1 s^{-1}). At the same time, at the strain rate of 0.001 and 0.01 s^{-1}, the ξ values are positive. At strain rate of 0.1 and 1 s^{-1}, the ξ values have negative value. Generally, when the ξ values are negative, the microstructure of the Ti2041 alloy may have defects at high strain rates and should be avoided during processing.

A three-dimensional distribution diagram of the instability parameter changing with deformation temperature, strain rate and strain is shown in Fig.11, where three strain sections are instability maps with strains of 0.3, 0.6, and 0.9. The black zone represents "stability", while the red zone is "instability". The instability zones gradually decrease with the increase of strain, mainly at high strain rate. The instability zones are mainly between 650~775 °C/0.056~1 s^{-1} and 850~900 °C/0.056~1 s^{-1}. The stability zones are mainly at low strain rate.

4.5 Processing map analysis

The corresponding material parameters m, η and ξ are calculated according Eq. (7), Eq. (9) and Eq. (10), respectively. Isolines of temperature and strain rates are plotted on the two-dimensional plane, which are the power dissipation map and the instability map. The two processing maps based on Prasad instability cri-

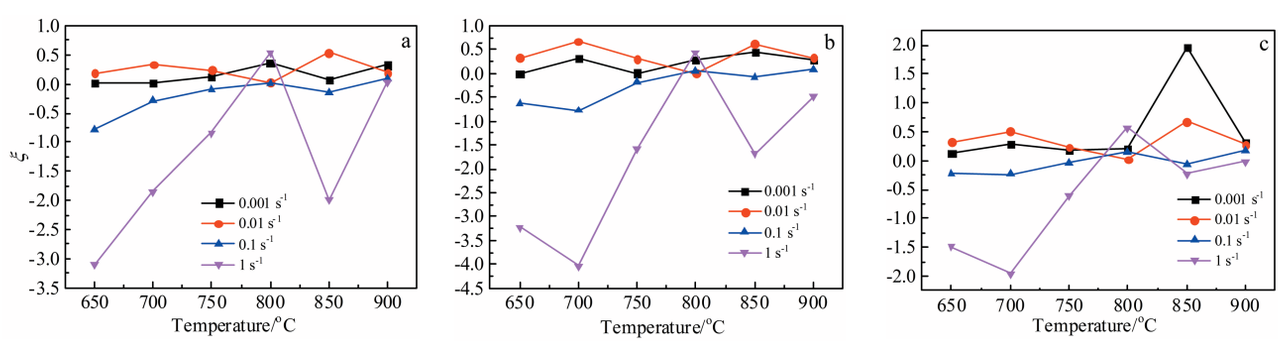

Fig.10 Influence of hot processing parameters on the value of ξ at different strains: (a) 0.3, (b) 0.6, and (c) 0.9

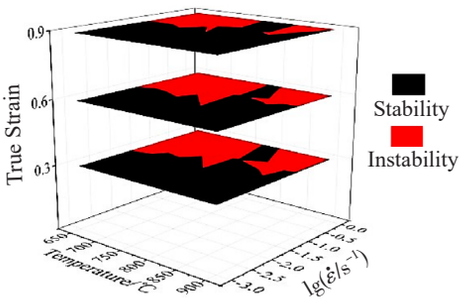

Fig.11 3D instability diagram of Ti2041 alloy

terion are obtained by superimposing them. As shown in Fig.12, the shadow zones in the processing map are the instability zones and the white zones are the safe machining zones.

It can be seen from the Fig.12 that the instability zone of the processing map changes under different strains. In actual processing, the material is in a non-uniform deformation. To avoid the instability of the structure, the instability of the material under different strains should be considered to ensure that the material has qualified performance after processing. According to the processing map, two instability zones can be recognized: the first instability zone occurs in the temperature range of 650~775 ℃ and strain rate range of 0.056~1 s^{-1}; the second instability zone is in the temperature range of 825~900 ℃ and strain rate range of 0.056~1 s^{-1}. In these zones, the corresponding power dissipation coefficient of materials is comparatively low, and the instability of adiabatic shear bands or local plastic flow tends to occur during deformation.

The power dissipation efficiency decreases a little with the increase of the strain in the processing map at the temperature of 760~825 ℃/strain rate of 0.001~0.01 s^{-1} and the temperature of 825~900 ℃/strain rate of 0.0032~0.056 s^{-1}. When the true strain is 0.3 and 0.9, the maximum values are 0.6 and 0.55, respectively. The power dissipation efficiency peak zone in the processing map often corresponds to the favorable deformation mechanism, such as superplasticity, dynamic recovery, and dynamic recrystallization. Favorable deformation mechanism should be given priority in the formulation of deformation parameters, and it is also considered that whether it is in the stability zone during the process of deformation. The favorable deformation mechanisms are at the temperature of 760~825 ℃/strain rate of 0.001~0.01 s^{-1} and temperature of 825~900 ℃/strain rate of 0.0032~0.056 s^{-1}. The ranges have the best processing parameters.

4.6 Microstructure verification

Previous studies have shown that the power dissipation efficiency and the instability zones in the processing map essentially represent the microstructure response under the condition of hot deformation [20, 29]. However, the processing map is insufficient to identify the available processing parameters due to the prediction inaccuracy of DMM theory [30,31]. Therefore, microstructural observation is often regarded as a necessary supplementary to determine the optimal parameters.

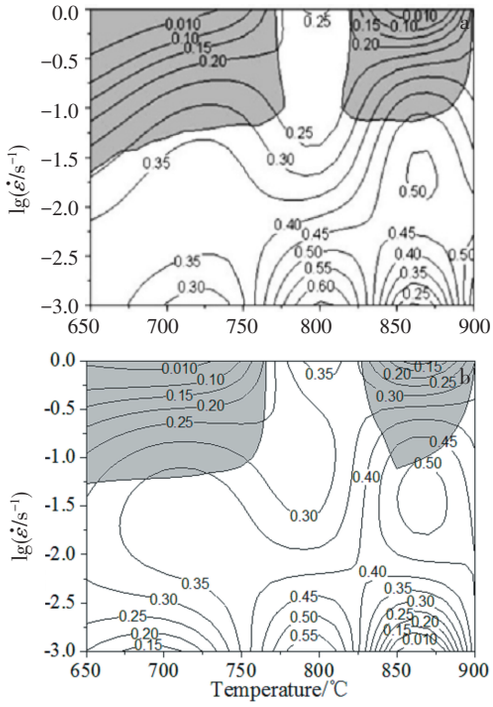

Fig.12 Processing maps of Ti2041 alloy at true strain of 0.3 (a) and 0.9 (b)

Fig.13~15 show the microstructures of the Ti2041 alloy under different deformation conditions. As shown in Fig.13, at the deformation temperature of 650 and 750 ℃, and the strain rate of 1 s^{-1}, flow localization phenomenon can be seen in the deformed structure. Due to the low hot conductivity of titanium alloys, the sample will have obvious hot effect during the deformation process and will easily generate adiabatic temperature rise, resulting in flow localization phenomena. However, material structure non-uniformity is relatively weak compared to adiabatic shear. The occurrence of flow localization means that the material has experienced severe uneven deformation, and the bearing capacity of the material is reduced or lost. This phenomenon is seen as a precursor to material failure and should be avoided during processing.

Mechanical instability occurs mainly in high temperature and high strain rate zones [22]. As shown in Fig.14, at the deformation temperature of 850 and 900 ℃and the strain rate of 1 s^{-1}, the coarse grains are elongated and different in size, which causes material anisotropy. It can also be seen that some grain boundaries are broken. It is obvious that the grains after compression are uneven and the mechanical instability occurs in the structure. Mechanical instability has a great influence on the mechanical properties of Ti2041 alloy, which reduces the processing properties of Ti2041 alloy. This zone should be avoided during processing.

Fig. 15 is the microstructure of stability zone at the true strain is 0.9. It is generally believed that dynamic recrystallization often occurs at high power dissipation efficiency and low strain rate [32,33]. As shown in Fig. 15a, at the temperature of 800 ℃ and the strain rate of 0.001 s^{-1}, it can be seen that dynamic

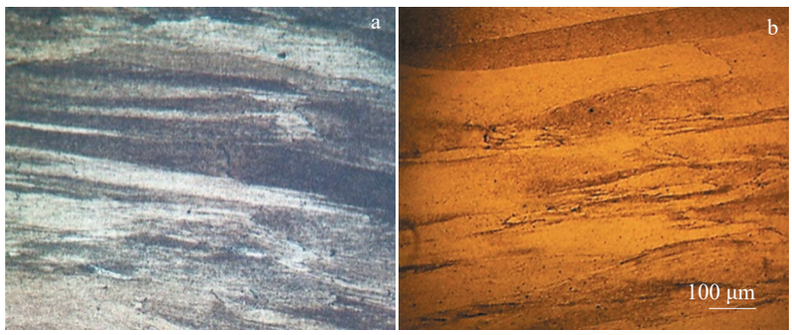

Fig.13 Microstructures of Ti2041 alloy under different deformation conditions: (a) 650 °C, 1s^{-1}; (b) 750 °C, 1s^{-1}

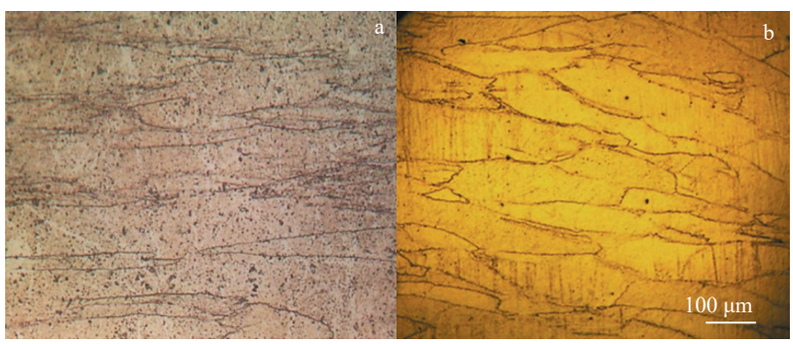

Fig.14 Microstructures of Ti2041 alloy under different deformation conditions: (a) 850 °C, 1s^{-1}; (b) 900 °C, 1 s^{-1}

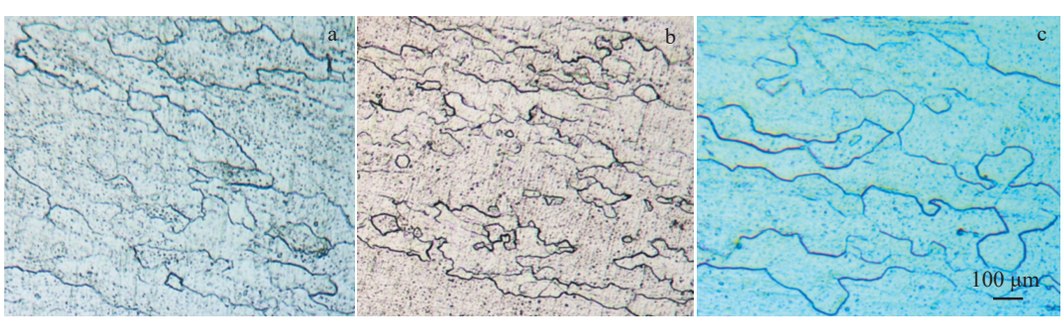

Fig.15 Microstructures of Ti2041 alloy under different deformation conditions: (a) 800 °C, 0.001 s^{-1}; (b) 850 °C, 0.01 s^{-1}; (c) 900 °C, 0.01 s^{-1}

recrystallization is dominant in this deformation condition and dynamic recrystallization grains can be seen in the structure. As shown in Fig.15b and 15c, at the temperatures of 850 and 900 °C and the strain rate of 0.01 s^{-1}, the number of recrystallized grains and grain size increase obviously. The dynamic recrystallization is more sufficient and the microstructure is uniform. In general, dynamic recrystallization is a beneficial deformation mechanism for the reconstruction of deformed structures.

Through processing map prediction and microstructure observation, it can see that the optimal processing parameters of Ti2041 alloy are deformation temperature of 760~825 °C/825~900 °C and strain rate 0.001~0.01 s^{-1}/0.0032~0.056 s^{-1}.

5 Conclusions

1) The flow stress of Ti2041 alloy during high temperature compression deformation has a close relationship with deformation temperature and strain rate. The flow stress will decrease with the increase of deformation temperature and the decrease of strain rate.

2) BP ANN models can well describe the flow behavior of the studied alloy. The correlation coefficient reaches 0.996 13, the average relative error is 4.498%, and the data points whose predictive deviation is within 10% reach 92.98%.

3) Hot processing parameters of the Ti2041 alloy exert a great impact on the isothermal deformation feature parameters, such as the strain rate sensitivity (m), power dissipation efficiency (η) and instability parameter (ξ) for establishment of the processing map. At the temperature of 800 °C and the strain rate of 0.001 s^{-1}, the m values reach the maximum value. The higher power dissipation zones mainly appear at deforma-

tion temperatures of 750~825 ℃/850~900 ℃ and the strain rate of 0.001~0.01 s^{-1}/0.001~0.1 s^{-1}. The lower power dissipation zones mainly appear when the temperature is 650~775 ℃ and the strain rate is 0.32~1 s^{-1}.

4) The processing maps of Ti2041 at different strains are obtained based on the power dissipation maps and instability maps. According to comprehensive processing map and microstructure analysis results, the instability zones are mainly flow localization (650~775 ℃/0.056~1 s^{-1}) and mechanical instability (825~900 ℃/0.056~1 s^{-1}). The optimum processing parameters are determined to be the deformation temperature of 760~825 ℃/825~900 ℃ and strain rate of 0.001~0.01 s^{-1}/0.0032~0.056 s^{-1}. The deformation mechanism of the corresponding zone is dynamic recrystallization.

References

1 Williams J C, Starke Jr E A. *Acta Materialia*[J], 2003, 51(19): 5775
2 Hao Y L, Li S J, Sun S Y *et al*. *Acta Biomaterialia*[J], 2007, 3(2): 277
3 Banerjee D, Williams J C. *Acta Materialia*[J], 2013, 61(3): 844
4 Li L, Li M Q. *Materials Science and Engineering A*[J], 2017, 698: 302
5 Lin Y C, Chen X M. *Materials & Design*[J], 2011, 32(4): 1733
6 Ma X, Zeng W D, Tian F *et al*. *Journal of Materials Engineering and Performance*[J], 2012, 21(8): 1591
7 Li H Y, Wei D D, Li Y H *et al*. *Materials & Design*[J], 2012, 35: 557
8 Huang C Q, Jia X D, Zhang Z W. *Materials*[J], 2018, 11(5): 855
9 Lin Y C, Huang J, Li H B *et al*. *Vacuum*[J], 2018, 157: 83
10 Li J Q, Liu J, Cui Z S. *Materials & Design*[J], 2014, 56: 889
11 Wu R H, Liu Y, Geng C *et al*. *Journal of Alloys and Compounds*[J], 2017, 713: 212
12 Sun Y, Feng X Y, Hu L X *et al*. *Journal of Alloys and Compounds*[J], 2018, 753: 256
13 Zang Q H, Yu H S, Lee Y S *et al*. *Materials Characterization*[J], 2019, 151: 404
14 Su Z X, Wan L, Sun C Y *et al*. *Materials Characterization*[J], 2016, 122: 90
15 Lin Y C, Nong F Q, Chen X M *et al*. *Vacuum*[J], 2017, 137: 104
16 Wan P, Wang K L, Zou H *et al*. *Journal of Alloys and Compounds*[J], 2019, 777: 812
17 Lin Y C, Chen X M, Wen D X *et al*. *Computational Materials Science*[J], 2014, 83: 282
18 Cai D Y, Xiong L Y, Liu W C *et al*. *Materials Characterization*[J], 2007, 58(10): 941
19 Liu J, Cui Z S, Li C X. *Journal of Materials Processing Technology*[J], 2008, 205(1): 497
20 Prasad Y V R K, Seshacharyulu T. *Materials Science and Engineering A*[J], 1998, 243(1): 82
21 Prasad Y V R K. *Journal of Materials Engineering and Performance*[J], 2003, 12: 638
22 Prasad Y V R K, Seshacharyulu T. *International Materials Reviews*[J], 1998, 43(6): 243
23 Lukaszek-solek A, Krawczyk J. *Materials & Design*[J], 2015, 65: 165
24 Ramanathan S, Karthikeyan R, Ganasen G. *Materials Science and Engineering A*[J], 2006, 441(1): 321
25 Wang H Y, Xue E S, Nan X L *et al*. *Scripta Materialia*[J], 2013, 68(5): 229
26 Suo T, Chen Y Z, Li Y L *et al*. *Materials Science and Engineering A*[J], 2013, 560: 545
27 Sun Y, Cao Z H, Wan Z P *et al*. *Journal of Alloys and Compounds*[J], 2018, 742: 356
28 Sun Y, Feng X Y, Hu L X *et al*. *Journal of Alloys and Compounds*[J], 2018, 753: 256
29 Zhang F, Sun J L, Shen J *et al*. *Materials Science and Engineering A*[J], 2014, 613: 141
30 Zhong L W, Gao W L, Feng Z H *et al*. *Journal of Materials Science & Technology*[J], 2019, 35(10): 2409
31 Cheng W L, Bai Y, Ma S C *et al*. *Journal of Materials Science & Technology*[J], 2019, 35(6): 1198
32 Liang H Q, Nan Y, Ning Y Q *et al*. *Journal of Alloys and Compounds*[J], 2015, 632: 478
33 Ma L X, Wan M, Li W D *et al*. *Journal of Alloys and Compounds*[J], 2019, 808: 151 759

基于BP神经网络和3D加工图的Ti2041合金的热变形行为

周 璇[1]，王克鲁[1]，鲁世强[1]，李 鑫[1]，欧阳德来[2]

(1. 南昌航空大学 航空制造工程学院, 江西 南昌 330063)

(2. 南昌航空大学 材料科学与工程学院, 江西 南昌 330063)

摘 要：通过热压缩实验研究了Ti2041合金的流动行为。利用BP神经网络建立的合金本构模型具有较高的精度，其相关系数达到0.99613，平均相对误差为4.498%，预测值偏差在10%以内的数据点达92.98%。在实验数据的基础上，研究了应变速率敏感因子、功率耗散和失稳参数。建立了加工图，通过加工图的预测和显微组织观察，失稳区主要为局部流动（650~775 ℃/0.056~1 s^{-1}）和机械失稳（825~900 ℃/0.056~1 s^{-1}），稳定区的变形机制主要为动态再结晶。结果表明：合适的变形参数为变形温度760~825 ℃/825~900 ℃，应变速率0.001~0.01 s^{-1}/0.0032~0.056 s^{-1}。

关键词：Ti2041合金；流动应力；本构模型；加工图；最佳工艺参数

作者简介：周 璇，男，1995年生，硕士生，南昌航空大学航空制造工程学院，江西 南昌 330063，电话：0791-83863039，E-mail：935593664@qq.com